Progress In Electromagnetics Research M, Vol. 108, 151–161, 2022

Simultaneous Measurement of Curvature and Temperature Based on a Simple Cascaded Fiber Interferometer

Fang Wang[1, 3], Yinghui Lu[1], and Yufang Liu[2, 3, *]

Abstract—An optical fiber sensor based on thin-core fiber (TCF) and no-core fiber (NCF) interference structures is presented and experimentally demonstrated to measure the curvature and temperature. The fabrication process of the sensor is simple and convenient, and the sensing part is formed by cascading a TCF and an NCF between two single-mode fibers. The dips at resonant wavelengths are generated in the optical transmission spectrum owing to mode interference. The experimental results indicate that an optical curvature sensitivity of $-5.76\,\mathrm{nm/m^{-1}}$ is achieved in the linear range of 0.9895–$3.2817\,\mathrm{m^{-1}}$ and that a temperature sensitivity of $0.18\,\mathrm{nm/°C}$ is obtained in the temperature range of 25–55°C. Additionally, the cross sensitivity problem is solved using the coefficient matrix measurement method, and the cross-sensitivity is as low as $0.0312\,\mathrm{m^{-1}/°C}$. Therefore, the sensor exhibits a highly reproducible technique and low cross sensitivity, which has a wide range of application prospects in the accurate measurement of mechanical arms and structural health monitoring.

1. INTRODUCTION

Optical fiber sensors have attracted more and more attention due to their inherent advantages such as simple structure, easy implementation, high sensitivity, chemical corrosion resistance, and are not easily affected by electromagnetic interference [1]. Furthermore, optical fiber sensors have been successfully used in monitoring physical quantities, such as temperature [2], strain [3], pressure [4], rotation [5], magnetic field [6], refractive index (RI) [7], relative humidity [8], and curvature [9–14]. The bending curvature of the structure is an important parameter for measuring the deformation of the object, and it is also an important optical parameter for optical fiber sensor. To date, bending measurement technology is commonly used for optical fiber sensing and has been applied in machinery, bridges, building structures, and high-precision instruments and equipment. After decades of development in optical fiber sensing technology, the requirements for optical fiber curvature sensors are increasing. Therefore, it is important to focus on reducing the production cost of optical fiber curvature sensors, simplifying their production process, and improving their measurement accuracy

Recently, studies have indicated that optical fiber curvature sensors with different structures, such as the Michelson interferometer [15, 16], Sagnac interferometer [17], fiber grating [18], modal interference [19], photonic crystal fiber (PCF) [20], and other sensors with various microstructures, are effective for curvature measurements [21–29]. For example, Ruan [17] fabricated a curvature sensor by splicing a piece of a multimode fiber between a single-mode fiber (SMF) and polarisation maintaining fiber. The measured curvature sensitivity was $11.6\,\mathrm{nm/m^{-1}}$ which is satisfactory. However, the sensor had an annular structure, making it inconvenient and difficult to use in precision instruments. Zhou et al. [20] proposed a sensor with a hybrid sensing structure for the simultaneous measurement

Received 7 December 2021, Accepted 7 February 2022, Scheduled 19 February 2022

* Corresponding author: Yufang Liu (liuyufang2005@126.com).

[1] College of Electronic and Electrical Engineering, Henan Normal University, Xinxiang 453007, China. [2] College of Physics, Henan Normal University, Xinxiang 453007, China. [3] Key Laboratory Optoelectronic Sensing Integrated Application of Henan Province, Xinxiang 453007, China.

of temperature and curvature. The sensor head was formed by cascading a PCF and fiber Bragg grating (FBG). Its curvature and temperature sensitivities were 4.06 nm/m^{-1} and only 6.3 pm/°C, respectively. However, the PCF is more expensive than a common optical fiber. Zhang et al. [15] fabricated a curvature sensor by splicing a tapered triple core fiber to a segment of a dual side hole fiber. Its curvature sensitivities can reach 53 and -57 nm/m^{-1} in the bending directions of $+x$ and $-x$, respectively. However, the tapered fibers are fragile, and the overall size of the tapered sensors can limit its application in the micro-environment. Zhu et al. [13] proposed a vector curvature sensor based on a single FBG. Its curvature sensitivities were 553.65 and -811.19 pm/m^{-1} under convex and concave bending. Fiber grating-type curvature sensors exhibit high sensitivity in certain curvature ranges, but the sensitivity is low when the curvature is considerably lower than 1. Additionally, it is difficult for single grating curvature sensors to distinguish the bending direction [30]. In this context, combined with our previous work of curvature sensor [9], we simplify the complexity of the fiber structure and propose an easily fabricated and low-cost sensor.

In this paper, we propose and demonstrate an optical fiber cascade sensor for simultaneous measurement of curvature and temperature. The sensor comprises a cascaded thin-core fiber (TCF) and no-core fiber (NCF) between input and output SMFs (STNS), which corresponds to the MZI. We employed the beam propagation method (BPM) to simulate the longitudinal and transverse optical field distributions of the STNS structure. Through the coefficient matrix method, the sensor achieves double-parameter measurement with a highly reproducible technique and high sensitivity. By fusion splicing optical fibers, better interference effect and measurement results were obtained, and the fabrication process is much simpler and more stable than those previously reported [9, 13, 15].

2. FABRICATION AND PRINCIPLE

2.1. Sensing Structure and Fabrication

A schematic diagram of the proposed sensor, which comprises segments of TCF and NCF cascaded with two SMFs (input/output), is shown in Fig. 1(a). The input and output SMFs of the sensor were purchased from YFCO, and the core and cladding were 8/125 µm in diameter. The TCF was a special fiber with a core diameter of 5 µm and a cladding diameter of 80 µm, and the NCF had a diameter of 125 µm. As shown in Fig. 1(a), the refractometer comprised two cascaded special optical fibers, with a sensing length of 20 mm.

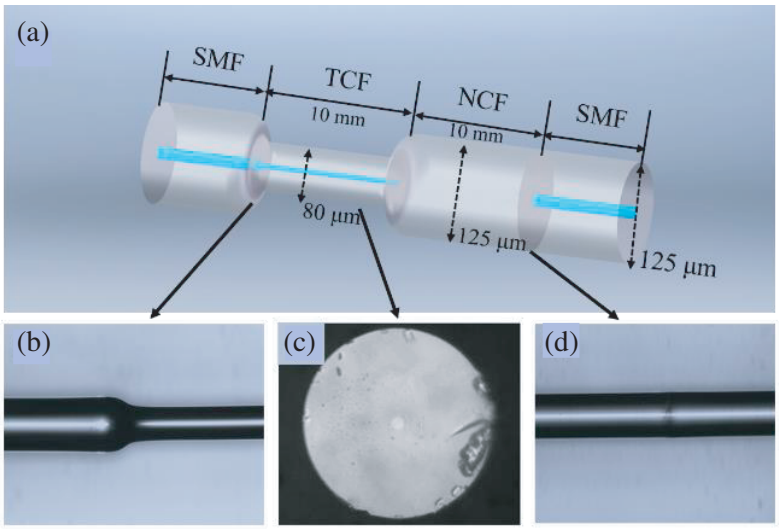

Figure 1. (a) Schematic of the composite modal interferometer. (b) Microscope image of the splicing points between the SMF and TCF. (c) Cross section of the TCF. (d) Microscope image of the splicing points between the SMF and NCF.

To fabricate the sensor, a TCF segment with a length of 10 mm was first coaxially spliced to one end of the NCF using a commercial fusion splicer (KL-280G, Jilong), which was equipped with an automatic splicing program. During the fusion process, the discharge intensity, discharge time, and loss were 100 bits 160 ms, and 0.01 dB, respectively. Figs. 1(b) and (d) show optical micrographs of the splicing points between the SMF and TCF, and the splicing points between the SMF and NCF, respectively. The cross section of the TCF under an electron microscope is shown in Fig. 1(c). The spliced sensor head was then connected to the input/output SMFs. The coating layer of the fiber was removed using acetone before the splicing. The output of a semiconductor optical amplifier produced from Conquer was connected to the output SMF, and the transmission spectrum of the STNS was observed via an optical spectrum analyser (OSA) connected to the sensor part.

To obtain a better interferometric spectrum, we tested the interference spectra of the three different optical fiber structures in the experiments. As shown in Fig. 2(a), no obvious interference dips can be observed in the SMF-TCF-SMF (STS) and SMF-NCF-SMF (SNS) structures. When the structure comprises STS and SNS splicing, the interference spectrum exhibits many interference peaks with good extinction ratios. Finally, the TCF and NCF lengths were selected as 10 mm in the experiment. The interferometric spectral pattern is shown in the inset of Fig. 2(b), and the free spectrum range (FSR) was equal to 22 nm. An MZI with an asymmetric cascade structure has the advantage of obtaining a better interferogram. Fast Fourier transform (FFT) was used to obtain the spatial frequency spectrum response, as shown in Fig. 2(b). In the spatial frequency spectrum, the number of interference modes and the power distribution were determined. The main strength peak at zero was related to the core modes. There were two main cladding modes and other weaker cladding modes. The interference between the fundamental mode and cladding modes was the main cause of the formation.

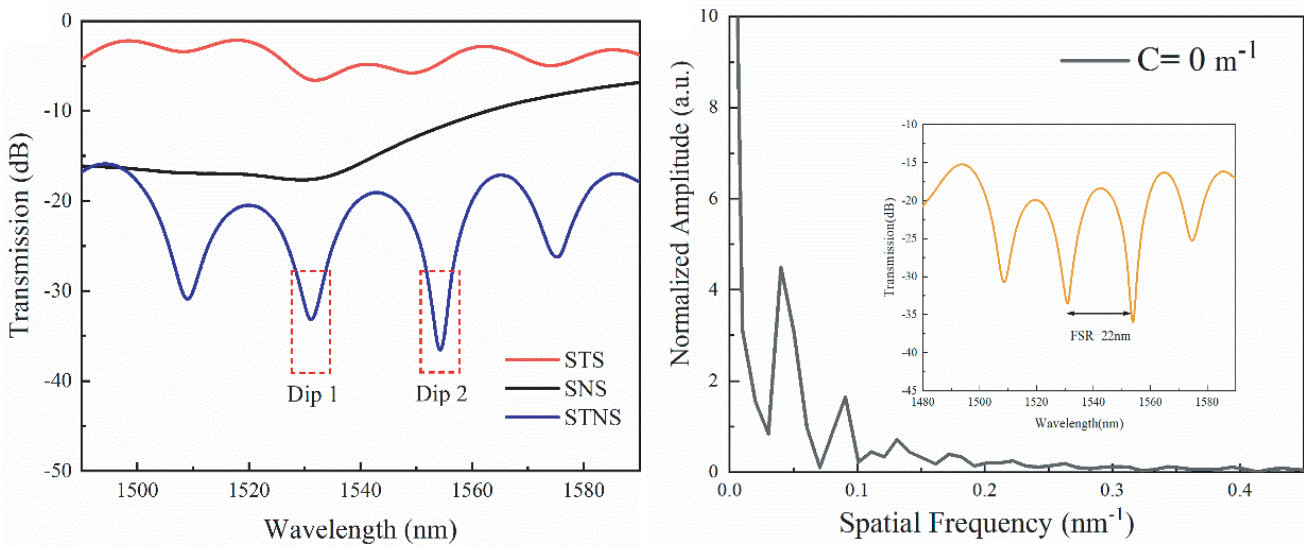

Figure 2. (a) Transmission spectra of the three different optical fiber structures. (b) Measured spatial frequency spectrum and transmission spectrum of the STNS.

2.2. Sensing Principle and Simulation

In this study, when the incident light passed through the first fusion joint of the SMF and TCF, the TCF cladding mode was effectively excited because of mode field mismatch. When light passed through the splicing point of the TCF and NCF, the high-order modes of the NCF were excited. Finally, light with all NCF modes gathered at the fusion joints of the NCF and SMF, and the interference occurred owing to the different propagation and excitation coefficients of the different modes.

The mathematical model of the interference region is established using the Jones matrix, by

simplifying the transmission intensity of the output interference spectrum. The transmission intensity at the output port is given as follows [12]:

$$I = I_{co} + \sum\nolimits_m I_{cl}^m + \sum\nolimits_m 2\sqrt{I_{co} + I_{cl}} \cos\left[\frac{2\pi \Delta_{n_{eff}L}}{\lambda}\right] \tag{1}$$

where I_{co} and I_{cl}^m represent the light intensities of the fundamental mode and m-order cladding, respectively. L represents the effective interference length (the sum of lengths of the NCF and TCF); λ represents the selected wavelength of the light source; and Δn_{eff} is the difference between the effective RIs of the core mode and the m-order cladding mode. The dip in the s-order interference spectrum is expressed as follows:

$$\lambda_s = \frac{2\left(n_{co} - n_{cl}^m\right)}{2s+1} L, \quad s = 1, 2, 3 \ldots \tag{2}$$

When the curvature is measured, the RI of the inner fundamental mode and the effective higher order mode of the fiber change owing to the bending of the fiber. According to Eq. (2), the FSR can be approximated as follows:

$$FSR \approx \frac{\lambda^2}{\Delta_{n_{eff}L} L} \tag{3}$$

When $\Delta_{n_{eff}L} = n_{co} - n_{cl}^m$, the FSR decreases with an increase in L.

During temperature measurement, the position of the interference spectrum changes significantly under the action of the thermal light coefficient and thermal expansion coefficient, and it can be expressed as follows [31]:

$$\Delta_\lambda = \left[(\varepsilon + \alpha)\, \Delta T\right] \lambda \tag{4}$$

where ε is the thermal optical coefficient of the core and cladding, α, the effective thermal expansion coefficient of the fiber, and λ the free space wavelength. The RI of the cladding and the effective sensing length of the sensor affect the temperature measurement. For simplicity, only the thermal-light coefficient and coefficient of thermal expansion were substituted into the formula.

In this study, according to the foregoing analysis, the BPM was used to obtain the optical field distribution of the proposed structure. The simulation parameters are presented in Table 1. Fig. 3(a) shows the beam propagation diagram of the MZI with a 10 mm long TCF 10 mm long NCF and a 1.555 µm wavelength.

Table 1. Main parameters of the simulation.

Fiber	RI of core	Core/cladding diameters (µm)	Length (µm)
TCF	1.4594/1.4378	5/80	10000
NCF	1.444	125	10000
Lead-in/out SMF	1.4502/1.445	9/125	20000

Because of the core mismatch and offset, the injected light is significantly diffused within the core and cladding of the TCF and NCF; the higher-order modes of the NCF are excited, and the power of light from the NCF is coupled to the lead-out SMF at the splice point. To demonstrate the change in the light field for the cascaded fiber interferometer, the transverse optical field distribution of the interferometer was simulated when the transmission distance changes [32]. The light field changes of the transverse optical field distribution are shown in Figs. 3(b)–(e). The simulated mode field distributions shown in Fig. 3 are based on the BPM at a wavelength of 1.555 µm. As shown in Fig. 3(b), the optical field at the SMF-TCF interface was mainly concentrated in the fiber core. From Figs. 3(c) and (d), the power of light in the optical fiber core was reduced, and the cladding was enhanced. This is because the core and cladding modes produced different effective RIs to form an interference spectrum. This is consistent with predictions of the foregoing theoretical analysis.

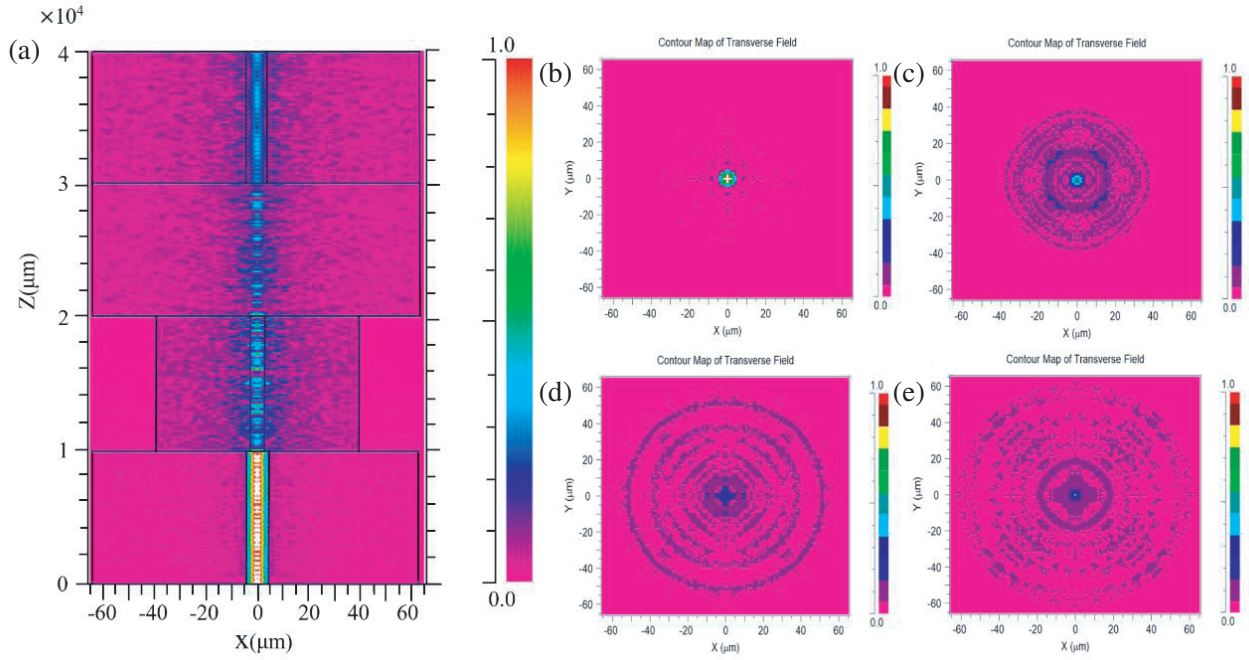

Figure 3. (a) Propagation field of the fiber with a wavelength of 1.555 nm, and the simulated transverse optical field distribution in the fiber interferometer under an input wavelength of 1.555 μm, (b) at $Z = 10,000$ μm, (c) $Z = 20,000$ μm, (d) $Z = 30,000$ μm, and (e) $Z = 40,000$ μm.

3. EXPERIMENT AND DISCUSSION

3.1. Curvature Experiment

The performance of the sensor, with the SMF-TCF-NCF-SMF structure for the curvature measurement, was experimentally evaluated using the setup shown in Fig. 4. The broadband light was launched from an SOA to the input SMF of the fiber structure (in the wavelength range of 1300–1700 nm), and the resolution of the OSA was 0.02 nm in the experiment. The transmission spectrum of the STNS sensor was measured with different curvatures. For the experimental curvature measurements, the sensing head was placed between two precision workstations. The distance between the workstations was 3.66 cm. The optical fibers were clamped on both sides of the translation stage. One side was fixed, and the other side was moved slowly in the horizontal direction (y-direction). The change in curvature range changed with the movement of the translation table. All experiments were performed at room temperature (25°C). The curvature of the sensor can be approximated as follows [10]:

$$C = \frac{1}{R} = \sqrt{\frac{24y}{(l_0 - y)^3}} \tag{5}$$

where C represents the curvature, l the initial distance between the two translation stages, R the radius of curvature, and y the movement distance of translation stage 1. In our experiment, the curvature measurement of the sensor relied on the three-dimensional moving stage. The length of translation stage 1 was increased in steps of 10 μm along the y-direction. The STNS sensor exhibited an excellent sensitivity response between the wavelength shift and curvature in the range of 0–4 m^{-1}

Figure 5 presents the interference spectra for different curvatures. As shown in Fig. 5(a), as the curvature increased in the range of 0.9895–3.2817 m^{-1}, the transmission spectrum of the MZI shifts to the left, and the extinction rate did not change significantly. The sensor head was pressured when translation stage 1 slowly moved in the y-direction, where the wavelength shifted owing to the interference between the fundamental mode and the cladding. The restoration experiment was conducted to study the stability and accuracy of the curvature response characteristics. Compared with

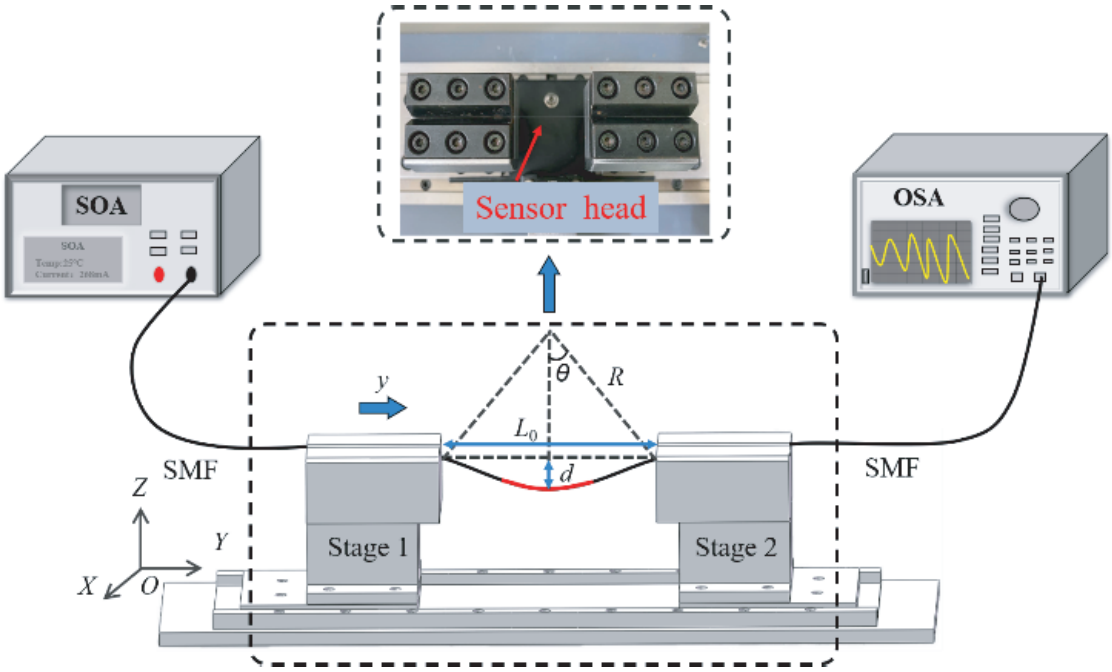

Figure 4. Experimental setup for curvature measurement.

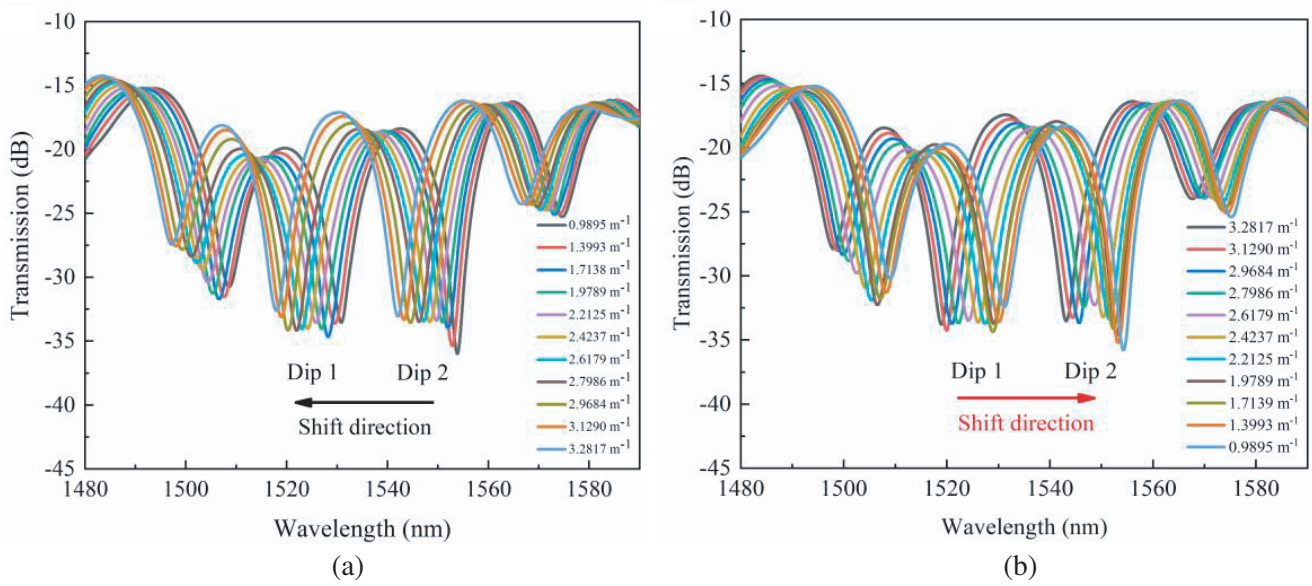

Figure 5. Interference spectra for curvature measurement of the STNS. (a) Interference spectra with an increasing curvature. (b) Interference spectra with a decreasing curvature.

extrusion, the translation table moved the same distance in the $-y$ direction and exhibited roughly the same interference spectrum as shown in Fig. 5(b). This indicates that the experiment has a relatively high repeatability.

Additionally, the detailed curvature performance of the two dips was investigated in the range of 0.9895–3.2817 m^{-1}. Observing the two dips revealed that the two interference recesses had different degrees of shift as the curvature increased, as shown in the inset of Fig. 6. Fig. 6 indicates that the response of the wavelength shifts of the two interferometric dips to the curvature was expressed by linear

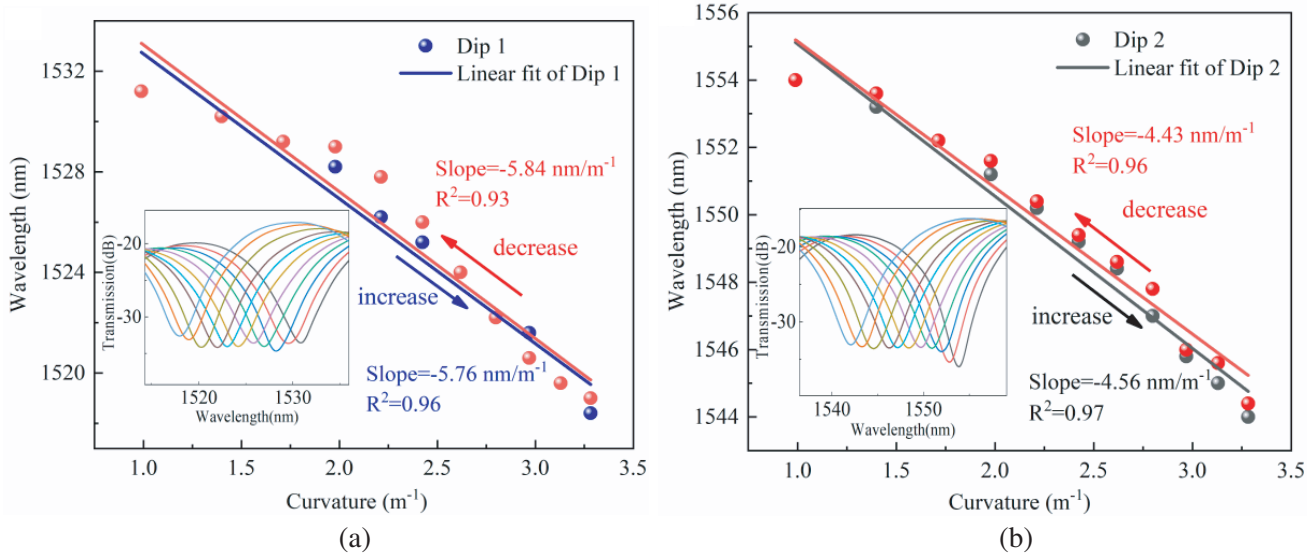

Figure 6. Curvature responses of the wavelength change at (a) dip 1 and (b) dip 2.

fitting, and the sensitivities were -5.76 and $-4.56\,\mathrm{nm/m^{-1}}$ for dips 1 and 2, respectively. Additionally, the sensitivities of dips 1 and 2 with a reduction in the curvature are provided. Comparing the linear fitting of the sensor with the increase and decrease in the curvature reveals that the sensor had a small error in the curvature measurement.

To further investigate the structural interference modes, we used FFT to study the frequency domain of the interference spectrum pattern. Fig. 7 shows the spatial frequency of the partial interference spectra in Fig. 5(a). According to the theoretical analysis, the sensor exhibits an excited cladding mode before and after bending. The diagram involved is mainly formed by the interference of the main core mode and cladding mode. The main peak in the spatial spectrum corresponds to the core mode, and its amplitude is constant. While multiple secondary peaks correspond to the cladding mode, it can be observed that the amplitude of the cladding mode decreased with the increasing curvature.

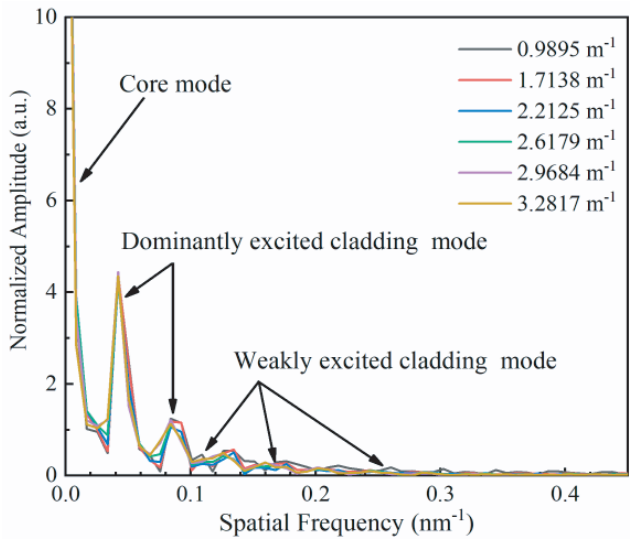

Figure 7. Spatial frequency spectra of the sensor under different curvature measurements.

3.2. Temperature Experiment

To measure the sensitivity of the interferometer to changes in the environmental temperature, the interferometer was heated using a thermostat (DHG-9036A). The thermostat was tested before the experiment to ensure that the entire sensing area could be heated evenly in the thermostat. In the experiment, the temperature was gradually increased from 25 to 55°C in steps of 5°C. When the temperature was increased to 60°C, the interference dip changes irregularly, so the proposed sensor operates in a limited temperature working range. The changes in the transmission spectra with the increasing temperature are shown in Fig. 8, and the temperature sensitivities were calculated via linear fitting. As shown in the inset of Figs. 8(a) and (b), the interference inclination in the interference spectra with increasing temperature shifts to longer wavelengths (red shift). The optical phase difference due to the RI changes in the core and cladding modes and the axial strain changes due to the thermal expansion synergistically affect the STNS, which shifted the wavelength of the interference dips. This is consistent with Eq. (4). The wavelength shifts caused by interference dips 1 and 2 (R^2 approaching 0.989 and 0.986) were plotted with respect to the temperature, and the linear fitting is shown in Fig. 8. As shown in the figure, temperature sensitivities of 0.18 and 0.12 nm/°C were obtained for dips 1 and 2, respectively.

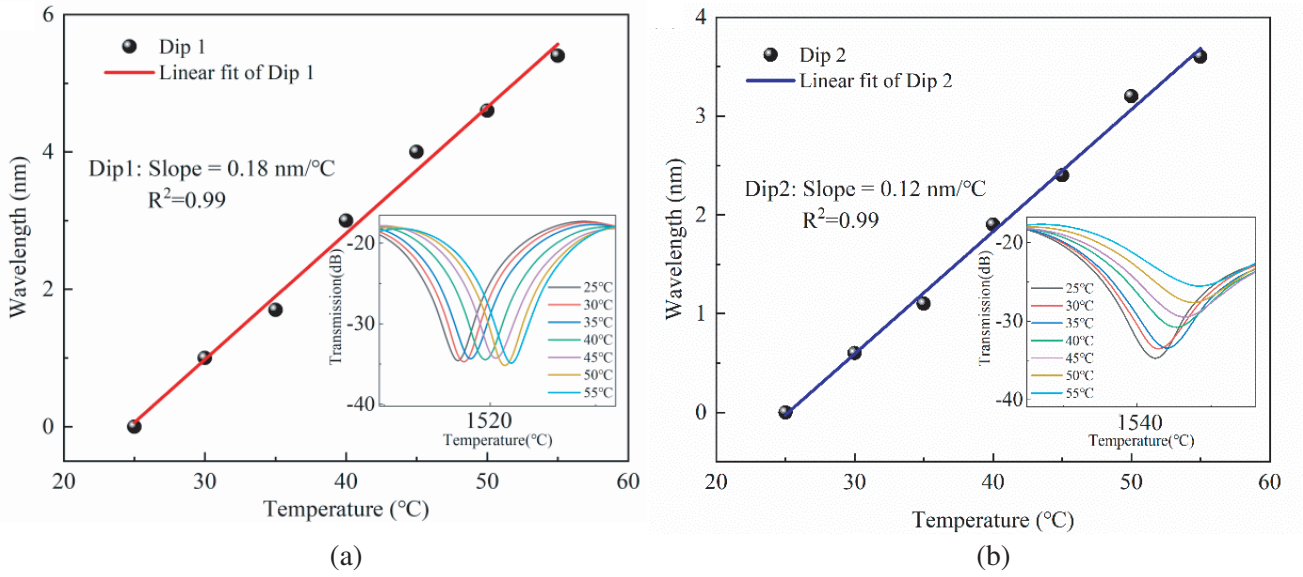

Figure 8. Linear fitting of the dips 1 and 2 wavelength shifts with respect to the temperature. The inset shows the transmission spectra in the temperature range of 25–55°C.

According to the experimental results for the curvature and temperature, the prospect of simultaneously measuring the two parameters is discussed. When dips 1 and 2 exhibit different sensitivities to the curvature and temperature measurements, the cross sensitivity caused by the temperature can be avoided in practical measurements. When two RIs are measured simultaneously, a matrix can be used for demodulation [33]. From the linear fitting results in Figs. 6 and 8, the sensitivities to curvature were −5.76 and −4.56 nm/m^{-1}, and the sensitivities to temperature were 0.18 and 0.12 nm/°C, respectively. Therefore, the changes in curvature and temperature were obtained using the following matrix:

$$\begin{bmatrix} \Delta C \\ \Delta T \end{bmatrix} = \begin{bmatrix} -4.56 & 0.18 \\ -5.76 & 0.12 \end{bmatrix}^{-1} \begin{bmatrix} \Delta\lambda_1 \\ \Delta\lambda_2 \end{bmatrix} \tag{6}$$

where ΔC and ΔT represent the changes in curvature and temperature, respectively, and $\Delta\lambda$ represents the wavelength shift of the dips. The curvature and temperature resolution of the interferometer at a wavelength resolution of 0.02 nm are 3.47×10^{-3} and 0.11°C, respectively. Therefore, simultaneous

Table 2. Comparison of optical fiber curvature sensors.

Sensor structure	Sensitivity of Curvature (nm/m^{-1})	Curvature ranges (m^{-1})	Sensitivity of Temperature (nm/°C)	Temperature range (nm/°C)	Ref.
Sensor based on a seven-core fiber	2.65	0.67–10	0.021	23–116	[11]
Curvature fiber sensor based on CFI	4.362	0–1.134	0.108	20–60	[12]
Curvature sensor based on the TCQSF	−1.83	0–0.94	-	-	[14]
Two-dimensional bending sensor with a three-core fiber	3.234	0–0.588	0.056	30–80	[18]
PCF-based interferometer and FBG	4.06	0–3	0.0063	20–100	[20]
MSM fiber structure with a biconical taper	4.4164	0.3487–0.4541	0.03393	20–65	[21]
Sensor based on Cascaded Fiber Interferometer	5.76	0.9895–3.2817	0.18	25–55	This work

measurements are feasible with the precondition of reducing the external measurement errors. Table 2 represents a comparison of the performance of optical fiber sensors with different structures, indicating the advantages of the proposed sensor. Compared with the other sensors, the proposed sensor exhibited better performance in the two parameters measurement and measurement range. Moreover, the proposed sensor has a low production cost and easy fabrication. Hence, it can have widespread applications in curvature sensing.

4. CONCLUSION

In summary, we proposed and experimentally demonstrated a simple cascaded fiber interferometer with low cross sensitivity and a highly reproducible fabrication technique which is suitable for simultaneously measuring curvature and temperature. The sensor head consists of a 10 mm long TCF and 10 mm long NCF spliced between SMFs. Experiments indicated that the sensitivities of the curvature and temperature can be measured by monitoring the wavelength shifts of the resonance dips in the interference spectra. The sensitivities of curvature and temperature were 5.76 nm/m^{-1} and 0.18 nm/°C, respectively. The proposed sensor is compact, convenient to operate, and can perform simultaneous double-parameter measurements. Thus it has significant potential in engineering systems.

ACKNOWLEDGMENT

This work was supported by the National Natural Science Foundation of China (NSFC) (62075057, 62075058); the Program for Innovative Research Team (in Science and Technology) in University of Henan Province (Grant No. 21IRTSTHN011); and Basic Research Project of Key Scientific Research Projects of the Higher Education Institutions of Henan Province (Grant No. 19B510006).

REFERENCES

1. Jang, M., J. S. Kim, S. H. Um, S. Yang, and J. Kim, "Ultra-high curvature sensors for multi-bend structures using fiber Bragg gratings," *Opt. Express*, Vol. 27, No. 3, 2074–2084, Feb. 2019.
2. Yang, W., C. Li, M. Wang, X. Yu, J. Fan, Y. Xiong, Y. Yang, and L. Li, "The polydimethylsiloxane coated fiber optic for all fiber temperature sensing based on the multi-thin-multi fiber structure," *IEEE Sens. J.*, Vol. 21, No. 1, 51–56, Jan. 2020.
3. Abbas, L. G., A. Zhou, F. Mumtaz, A. Muhammad, Y. Dai, and R. Parveen, "Temperature and strain sensing with hybrid interferometer," *IEEE Sens. J.*, Vol. 21, No. 23, 26785–26792, Dec. 2021.
4. Hou, Y., J. Wang, X. Wang, Y. Liao, L. Yang, E. Cai, and S. Wang, "Simultaneous measurement of pressure and temperature in seawater with PDMS sealed microfiber Mach-Zehnder interferometer," *J. Lightwave Technol.*, Vol. 38, No. 22, 6412–6421, Nov. 2020.
5. Azmi, A., A. Abdullah, M. Noor, M. Ibrahim, R. Ibrahim, T. Tan, and J. Zhang, "Dynamic bending and rotation sensing based on high coherence interferometry in multicore fiber," *Opt. Laser Technol.*, Vol. 135, 106716, Mar. 2021.
6. Zhang, X., B. Liu, H. Zhang, J. Wu, B. Song, and C. Wang, "A magnetic field sensor based on a dual S-tapered multimode fiber interferometer," *Meas. Sci. Technol.*, Vol. 29, No. 7, 075103, Jul. 2018.
7. Wang, F., K. Pang, T. Ma, X. Wang, and Y. Liu, "High-sensitivity and temperature-insensitive refractometer based on TNHF structure for low-range refractive index measurement," *Progress In Electromagnetics Research*, Vol. 166, 167–175, 2019.
8. Chen, W., Z. Chen, Y. Zhang, and H. Li, "Fiber sensor for relative humidity measurement at water absorption band of 2 μm," *Meas. Sci. Technol.*, Vol. 31, No. 3, 035101, Dec. 2019.
9. Wang, F., L. Zhang, X. Wang, T. Ma, K. Yu, and Y. Liu, "A high-sensitivity sensor based on tapered dispersion compensation fiber for curvature and temperature measurement," *Opt. Commun.*, Vol. 481, 126534, Oct. 2020.
10. Zhao, Y., C. Cai, and X. Li, "Temperature-insensitive optical fiber curvature sensor based on SMF-MMF-TCSMFMMF-SMF structure," *IEEE T. Instrum. Meas.*, Vol. 66, No. 1, 141–147, Jan. 2017.
11. Zhou, Y., Y. Wang, H. Liu, J. Chen, P. Yang, L. she, F. Chen, J. Shao, Z. Guan, and Z. Zhang, "High-sensitive bending sensor based on a seven-core fiber," *Opt. Commun.*, Vol. 483, 126617, Mar. 2021.
12. Dong, S., B. Dong, C. Yu, and Y. Guo, "High sensitivity optical fiber curvature sensor based on cascaded fiber interferometer," *J. Lightwave Technol.*, Vol. 36, No. 4, 1125–1130, Feb. 2018.
13. Zhu, F., Y. Zhang, Y. Qu, W. Jiang, H. Su, Y. Guo, and K. Qi, "Stress-insensitive vector curvature sensor based on a single fiber Bragg grating," *Opt. Fiber. Technol.*, Vol. 54, No. 102133, Jan. 2020.
14. Fu, X., J. Wen, Y. Zhang, D. Wang, F. Liu, H. Xie, G. Fu, and W. Bi, "Experimental and theoretical analysis of curvature sensor based on cladding mode resonance with triple cladding quartz specialty fiber," *Opt. Commun.*, Vol. 429, 5–11, Dec. 2018.
15. Zhang, S., Y. Liu, H. Guo, A. Zhou, and L. Yuan, "Highly sensitive vector curvature sensor based on two juxtaposed fiber Michelson interferometers with Vernier-like effect," *IEEE Sens. J.*, Vol. 19, No. 6, 2148–2154, Mar. 2019.
16. Zhao, Y., A. Zhou, H. Guo, Z. Zheng, Y. Xu, C. Zhou, and L. Yuan, "An integrated fiber michelson interferometer based on twin-core and side-hole fibers for multiparameter sensing," *J. Lightwave Technol.*, Vol. 36, No. 4, 993–997, Feb. 2018.

17. Ruan, J., "Fiber curvature sensor based on concave-heterotypic cascaded fiber Sagnac interferometer," *Microw. Opt. Techn. Let.*, Vol. 62, No. 11, 3645–3649, Nov. 2020.
18. Wang, S., W. Zhang, L. Chen, Y. Zhang, P. Geng, Y. Zhang, T. Yan, L. Yu, W. Hu, and Y. Li, "Two-dimensional micro bend sensor based on long-period fiber gratings in an isosceles triangle arrangement three-core fiber," *Opt. Lett.*, Vol. 42, No. 23, 4938–4941, Dec. 2017.
19. Oliveira, R., J. Osorio, S. Aristilde, L. Bilro, R. Nogueira, and C. Cordeiro, "Simultaneous measurement of strain, temperature and refractive index based on multimode interference, fiber tapering and fiber Bragg gratings," *Meas. Sci. Technol.*, Vol. 27, No. 7, 075107, Jul. 2016.
20. Zhou, Y., W. Zhou, C. Chan, W. Wong, L. Shao, J. Cheng, and X. Dong, "Simultaneous measurement of curvature and temperature based on PCF-based interferometer and fiber Bragg grating," *Opt. Commun.*, Vol. 284, No. 24, 5669–5672, Dec. 2011.
21. Wo, J., Q. Sun, X. Li, D. Liu, and P. Shum, "Biconical-taper-assisted fiber interferometer with modes coupling enhancement for high-sensitive curvature measurement," *Appl. Phys. B — Lasers O.*, Vol. 115, No. 1, 1–8, Apr. 2014.
22. Sun, X., H. Du, X. Dong, Y. Hu, and J. Duan, "Simultaneous curvature and temperature sensing based on a novel Mach-Zehnder interferometer," *Photonic Sens.*, Vol. 10, No. 2, 171–180, Jun. 2020.
23. Gutiérrez Gutiérreza, J., J. Sierra-Hernandez, M, Vargas-Trevino, E. Lopez-Apreza, C. Romero-Salazar, O. Hernandez-Flores, J. Estudillo-Ayala, and R. Rojas-Laguna, "A curvature sensing setup based on an asymmetric concatenated tapered Mach-Zehnder interferometer," *Opt. Laser Technol.*, Vol. 132, 106490, Dec. 2020.
24. Chen, E., B. Dong, Y. Li, X. Wang, Y. Zhao, W. Xu, W. Zhao, and Y. Wang, "Cascaded few-mode fiber down-taper modal interferometers and their application in curvature sensing," *Opt. Commun.*, Vol. 475, 126274, Nov. 2020.
25. Cheng, H., S. Wu, Q. Wang, S. Wang, and P. Lu, "In-line hybrid fiber sensor for curvature and temperature measurement," *IEEE Photon. J.*, Vol. 11, No. 6, 6803311, Dec. 2019.
26. Zhao, Y., L. Cai, and X. Li, "High sensitive modal interferometer for temperature and refractive index measurement," *IEEE Photonic Tech. L.*, Vol. 27, No. 12, 1341–1344, Jun. 2015.
27. Yu, F., P. Xue, and J. Zheng, "Enhancement of refractive index sensitivity by bending a core-offset in-line fiber Mach-Zehnder interferometer," *IEEE Sens J.*, Vol. 19, No. 9, 3328–3334, May 2019.
28. Zhao, Y., M. Chen, F. Xia, L. Cai, and X. Li, "Small curvature sensor based on butterfly shaped Mach-Zehnder interferometer," *IEEE T. Electron. Dev.*, Vol. 64, No. 11, 4644–4649, Nov. 2017.
29. Zhang, Y., W. Zhang, Y. Zhang, S. Wang, L. Yu, and Y. Yan, "Simultaneous measurement of curvature and temperature based on LP11 mode Bragg grating in seven-core fiber," *Meas. Sci. Technol.*, Vol. 28, No. 5, 055101, May 2017.
30. Wang, Q. and Y. Liu, "Review of optical fiber bending/curvature sensor," *Measurement*, Vol. 130, 161–176, Dec. 2018.
31. Zheng, Y., X. Yang, W. Feng, and W. Fan, "Optical fiber refractive index sensor based on SMF-TCF-NCF-SMF interference structure," *Optik*, Vol. 226, 169500, Jan. 2021.
32. Lu, H., X. Wang, S. Zhang, F. Wang, and F. Liu, "A fiber-optic sensor based on no-core fiber and Faraday rotator mirror structure," *Opt. Laser Technol.*, Vol. 101, 507–514, May 2018.
33. Raji, Y. M., H. S. Lin, S. A. Ibrahim, M. R. Mokhtar, and Z. Yusoff, "Intensity-modulated abrupt tapered Fiber Mach-Zehnder Interferometer for the simultaneous sensing of temperature and curvature," *Opt. Laser Technol.*, Vol. 86, 8–13, Dec. 2016.